communications biology

A Nature Portfolio journal

Article

https://doi.org/10.1038/s42003-025-07761-1

Structural insights into calcium-dependent CIB2-TMC1 interaction in hair cell mechanotransduction

Yahong Li[1,3], Jiasheng Chen[1,3], Wenli Jiang[1], Jin Ye[1], Xuan Zhang[2] & Chao Wang[1,2]

Calcium- and integrin-binding protein 2 (CIB2) plays a crucial role in mechanoelectrical transduction (MET) in cochlear hair cells, particularly in modulating the function and localization of the core components of MET channels TMC1/2. CIB2, along with its homolog CIB3, interacts with TMC1/2 through two distinct sites. Here, our study unveils CIB2/3's role as a calcium sensor in its interaction with TMC1. Utilizing X-ray crystallography, we elucidate the high-resolution structure of the mammalian CIB2-TMC1 complex. Structural analyses reveal that cation-bound CIB2 forms a negatively charged surface that aligns with a positively charged surface on the TMC1 N-terminus. Moreover, our data suggest that Ca^{2+} modulates CIB2's interaction with both the N-terminal domain and the loop 1 region of TMC1, and that Ca^{2+}-bound CIB2 is capable of simultaneously binding to both regions of TMC1. Critically, we examine pathogenic variants of CIB2 associated with hearing loss, discovering that these variants have differential impacts on CIB2's interactions with TMC1's dual binding sites, displaying diminished calcium-binding affinities for several of these CIB2 mutations. These findings provide a deeper understanding of the molecular mechanisms underlying CIB2 function and its implications in hearing loss, offering potential avenues for therapeutic interventions in deafness.

In mammals, the perception of sound is initiated through mechanoelectrical transduction (MET) in cochlear hair cells. These cells, embedded within the organ of Corti, are characterized by their apical stereocilia, arranged in a staircase-like formation[1]. Crucial to MET is the role of specialized channels located at the tips of these stereocilia, responsible for transducing mechanical stimuli into electrical signals. Identifying the molecular constituents of these MET channel complex has been a focal point of auditory research. TMC1 and TMC2, integral membrane proteins situated at the tip of the shorter-row stereocilia, have been identified as principal components of these channels[2–4]. Their significance is further underscored by findings revealing their pore-forming abilities and high Ca^{2+} permeability[5–7], and the association of specific TMC1 mutations with hereditary deafness[8].

The functionality of MET channels is intricately regulated by auxiliary subunits, among which Calcium- and integrin-binding protein 2 (CIB2) plays a pivotal role. This EF-hand protein, capable of binding both Mg^{2+} and Ca^{2+}, is predominantly expressed in cochlear hair cells[9–11], and reported to interact with the N-terminal cytoplasmic region of TMC1/TMC2[9,12,13]. Its importance is further underscored by the significant morphological defects in stereocilia and the association of CIB2 mutations with non-syndromic deafness[9,14]. Alongside its homolog CIB3, CIB2 is instrumental in regulating the transport and localization of TMC1 within stereocilia[15]. Recent studies have elucidated the interaction of CIB3 with TMC1, identifying a novel CIB-binding site within TMC1's first cytoplasmic loop between transmembrane domain 2 and 3[15]. Moreover, recent studies provided evidences that Piezo1 and Piezo2 form functional units capable of generating mechanoelectrical transduction (MET) currents. These units have been shown to interact with both mouse TMC1/TMC2 and CIB2, thereby suggesting that Piezo may constitute a part of the MET channel complex[16].

Further insights into the CIB2-TMC interaction have been garnered from structural analyses using cryo-electron microscopy (cryo-EM) with the endogenously purified *C. elegans* TMC-1 and TMC-2 complex[17,18]. The findings from these studies have highlighted two distinct binding sites for CALM-1 on TMC-1, consistent with previous biochemical and structural

[1]Department of Neurology, the First Affiliated Hospital of USTC, Center for Advanced Interdisciplinary Science and Biomedicine of IHM, Hefei National Research Center for Physical Sciences at the Microscale, Division of Life Sciences and Medicine, University of Science and Technology of China, Hefei, China. [2]Ministry of Education Key Laboratory for Membrane-less Organelles and Cellular Dynamics, Biomedical Sciences and Health Laboratory of Anhui Province, University of Science and Technology of China, Hefei, China. [3]These authors contributed equally: Yahong Li, Jiasheng Chen. e-mail: cwangust@ustc.edu.cn

findings[9,15]. However, the structural and mechanistic nuances of the CIB2-TMC1 interaction in mammals remain to be fully elucidated. This gap in understanding is due in part to the multifunctional nature of nematode TMC1, which exhibits diverse roles across various neuronal and muscular systems, such as functioning in mechanosensation in OLQ neurons, as a pH sensor in ASH neurons, and as a leak channel in HSN neurons and vulval muscles[12,19,20]. Therefore, the mechanistic details and structural basis of mammalian CIB2/TMC1 interaction have remained poorly understood to date, and a comprehensive understanding of the mammalian CIB2-TMC1 interaction, particularly from a structural perspective, is crucial for advancing our knowledge of MET processes and their implications in auditory function and dysfunction.

In this study, we meticulously examined the binding and structural interactions between TMC1 and CIB2. Our biochemical assays revealed that the 86-136 amino acid segment within the TMC1's N-terminus is crucial for its robust interaction with both CIB2 and CIB3. We successfully resolved the high-resolution crystal structure of the mammalian CIB2-TMC1 complex, offering unprecedented insights into this interaction. The structural analyses highlight that electrostatic interactions and hydrogen bonding predominantly facilitate the complex formation, with hydrophobic interactions providing additional stabilization. Significantly, our findings also reveal a critical role for Ca^{2+} in the regulation of CIB2-TMC1 interaction, as elevated binding affinity between Ca^{2+}-bound CIB2 and the N-terminus of TMC1. Interestingly, in the absence of Ca^{2+}, no interaction was observed between CIB2 and the loop 1 region of TMC1. This disparity underscores the distinct nature of the two CIB2-binding sites within the CIB2-TMC1 complex. Furthermore, we evaluated several CIB2 deafness-related mutations and observed that these variants affected the binding to TMC1 differentially, coupled with a diminished Ca^{2+} binding affinity. These results collectively contribute valuable insights into the role of calcium ions in the formation of the MET complex, thereby advancing our understanding of the molecular mechanisms underlying mechanotransduction in the mammalian inner ear.

Results

Characterization of the CIB2-TMC1 interaction

The mammalian calcium- and integrin-binding protein family comprises four members, known as CIB1-4[21]. CIB2 has been identified as the closest homolog to CIB3 (Supplementary Fig. 1a, b). Previous studies have revealed that a segment within the N-terminal cytoplasmic region of TMC1 serves as the binding domain for CIB2[9,12,13]. We first systematically confirmed and delineated the specific interacting fragments of human TMC1 binding to full-length human CIB2 using isothermal titration calorimetry (ITC) assays with highly purified proteins. The results unequivocally established that the region encompassing residues 86–136 of human TMC1, denoted as "CBD-1" (CIB binding domain-1), is not only essential but also sufficient for binding to CIB2 (Fig. 1a, b, d). Notably, three fragments including 105–136, 116–136, and 86–116 exhibited no binding to CIB2 (Fig. 1b, Supplementary Fig. 2a–c). CIB2 exhibited binding to the 95-136 fragment of TMC1 with a dissociation constant (K_d) of approximately 4.6 μM, showing a 14-fold weaker affinity compared to the longer TMC1 CBD-1 (Fig. 1b, Supplementary Fig. 2d). Moreover, we utilized analytical gel filtration chromatography (AGFC) coupled with a static light scattering assay to ascertain the binding ratio between CIB2 and TMC1 CBD-1. The results revealed that both CIB2 and TMC1 CBD-1 exist as monomers, forming a complex with a 1:1 binding stoichiometry (Fig. 1c).

Subsequent ITC assays were conducted to evaluate the binding affinities between TMC1 CBD-1 and all members of the CIB family (Fig. 1e). The experiments demonstrated a robust binding between TMC1 and CIB2 and CIB3, while a notably weak interaction was observed with CIB1 and no binding was detected with CIB4 (Fig. 1d, e, Supplementary Fig. 3a–c). AGFC assays further revealed the interaction between CIB3 and TMC1, with CIB3 existing in heterogeneous states (Supplementary Fig. 3d). Consolidating this data, we inferred that the direct interaction between TMC1 and CIB2 was marginally stronger than that with CIB3. Taken together, these findings underscore a robust interaction between CIB2 and TMC1, with the residues 86–136 of TMC1 mediating this interaction in a 1:1 binding ratio.

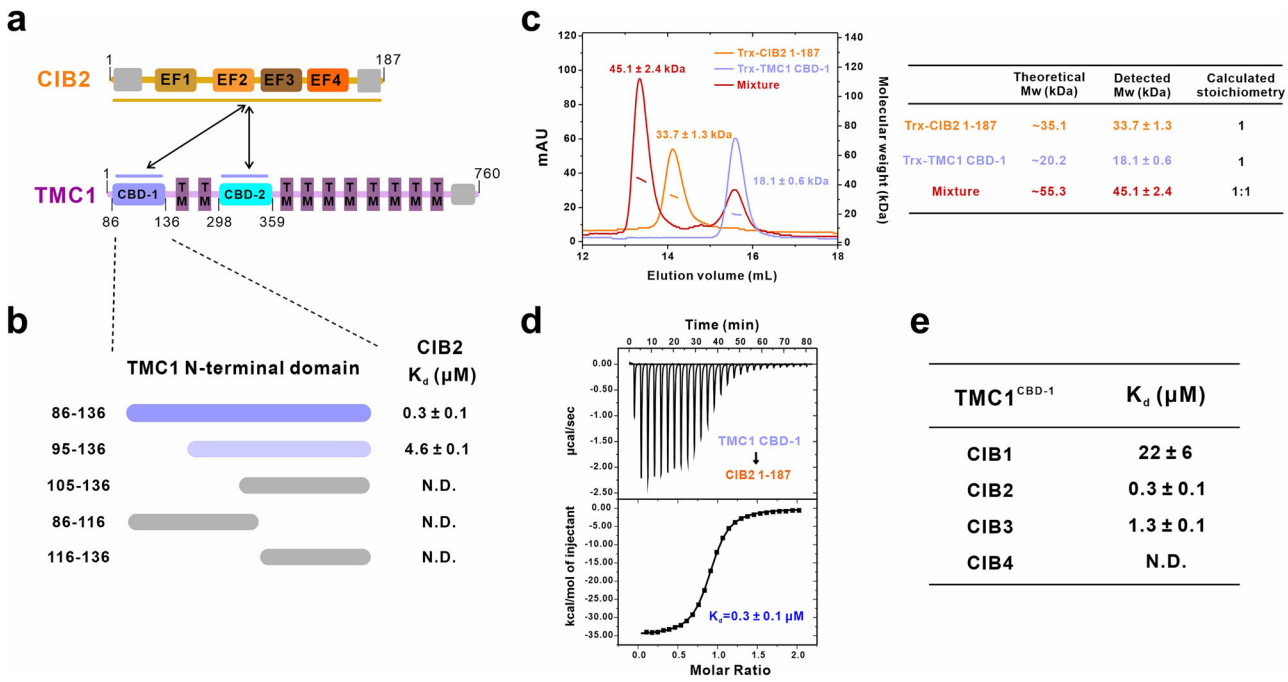

Fig. 1 | CIB2 binds strongly to TMC1^{CBD-1} at a 1:1 molar ratio. a Schematic diagram showing the domain organizations of CIB2 and TMC1. In this drawing, the interactions between CIB2 and TMC1 are indicated by two 2-way arrows. The CIB2 binding domain of TMC1 are highlighted in indigo and cyan. **b** ITC-based mapping of the CBD-1 domain in the TMC1 N-terminal region. The complete TMC1^{CBD-1} identified is highlighted in indigo. N.D. refers to not detectable. **c** Analytical gel filtration chromatography analysis coupled with static light scattering analysis of CIB2 1-187 (orange line), TMC1^{CBD-1} (pastel blue line), and the CIB2-TMC1 complex (red line), indicating that CIB2 and TMC1 form a stable 1:1 complex in solution. **d** ITC-based measurement of the binding affinity of CIB2 1-187 with TMC1^{CBD-1}. The Kd error is the fitting error obtained using one-site binding kinetics model in Origin 7.0 to fit the ITC data. **e** The measured binding affinities between CIB family proteins and TMC1^{CBD-1} from ITC-based binding assays.

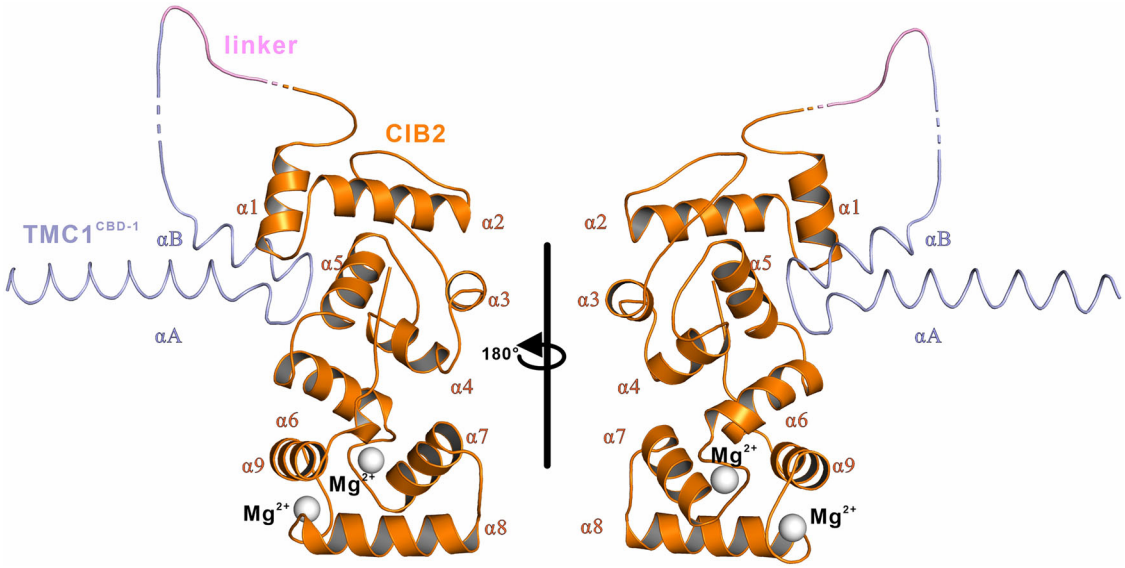

Fig. 2 | Overall crystal structure of CIB2 in complex with TMC1^{CBD-1} domain. Ribbon representation model showing the overall structure of the CIB2-TMC1^{CBD-1} complex. In this drawing, CIB2 is shown in orange, and TMC1 is shown in light blue, the fusion linker between CIB2 and TMC1 is shown in pink. Mg^{2+} are shown in gray. CIB2 contains 9 α-helical domains, denoted by α1-α9. TMC1^{CBD-1} contains 2 α-helices, denoted by αA and αB. The interface mediating the CIB2-TMC1 complex formation involves the α1 and α5 helices of CIB2, as well as the loop that links the α1 and α2 helices, all of which engage in the interactions with TMC1. The coordinates and structure factors of the CIB2 and TMC1 complex have been deposited to the Protein Data Bank under the accession code number 8XOQ.

Overall crystal structure of CIB2 in complex with TMC1^{CBD-1}

To elucidate the assembly mechanisms of the mammalian CIB2-TMC1 complex, we sought to crystallize the protein complex using different versions of complex preparations including mixing the two proteins at a 1:1 ratio or creating fusion proteins. Through comprehensive screening, we determined the crystal structure, in which TMC1^{CBD-1} was C-terminally fused to full-length CIB2. We resolved the complex structure to a 2.4 Å resolution using molecular replacement (Fig. 2, Table 1). In line with our biochemical data, the final structure model encompasses amino acids 3 to 187 of CIB2 and 86 to 127 of TMC1.

In this structure, CIB2 adopts a superhelical fold with four EF-hands. Notably, only the third and fourth EF-hands of CIB2 are functional in cation response (Fig. 2). This configuration closely resembles its homologous proteins of CIB1 and CIB3[15,21]. Interestingly, under calcium conditions (10 mM $CaCl_2$) used during purification and magnesium conditions (200 mM $MgCl_2$) used in the crystallization solution, we observed magnesium ions (Mg^{2+}) binding to EF3 and EF4, rather than calcium ions (Fig. 2, Supplementary Fig. 4). The measurement results indicate that the distance between cation and the ligating oxygen atoms is approximately 2 Å in CIB2 EF-hand structure, which aligns with the typical range for Mg^{2+}, and the distance for Ca^{2+} is found to be larger[22,23]. This preference for Mg^{2+} may be attributed to the inherently higher binding affinity of Mg^{2+} compared to Ca^{2+} for CIB2[24,25]. The interface between CIB2 and TMC1 comprises the α1-helix, α5-helix, and loop connecting the α1 and α2 helices of CIB2, which interact with TMC1 (Fig. 2). TMC1 anchors via two α-helices - an N-terminal αA extending over 23 residues and a C-terminal αB comprising 13 residues, linked by a 6-residue connector (amino acids 108-113).

Detailed structure characterization at the CIB2-TMC1^{CBD-1} interface

Electrostatic potential analysis revealed a negatively charged central pocket on the surface of CIB2, corresponding to its binding site with TMC1 (Fig. 3a). Subsequent structural investigations indicated that the CIB2-TMC1^{CBD-1} interface is predominantly stabilized via electrostatic interactions and hydrogen bonding. In particular, D90 and D93 from CIB2 form salt bridges with K112 and K116 from TMC1, respectively (Fig. 3b). Additionally, E11 from CIB2 engages in a charge-charge interaction with K121 from TMC1 (Fig. 3b). The side chain of K107 from TMC1 participates in a cation-π interaction with F21 of CIB2 (Fig. 3c, d). Several hydrogen bonds further contribute to the binding affinity and specificity, including those between Q17 and T20 from CIB2 and K107 and K116 of TMC1 (Fig. 3e), as well as between D93 from CIB2 and M113 from TMC1 (Fig. 3e). Furthermore, the side chain of M113 from TMC1 insert into a hydrophobic pocket formed by I27, L30, F88, and V92 from CIB2, enhancing the stability of the complex assembly (Fig. 3f).

To assess the significance of key residues at the CIB2-TMC1^{CBD-1} interface, we conducted mutational studies and examined the impact on CIB2-TMC1^{CBD-1} binding using AGFC and ITC. In line with our structural findings, mutations that disrupted pivotal interactions resulted in weakened or nullified binding between CIB2 and TMC1^{CBD-1} (Fig. 3g). Substituting D93 from CIB2 with alanine remarkably reduced TMC1 binding (Fig. 3g, Supplementary Fig. 5a, g), while the D90R variant from CIB2 also significantly weakened the interaction (Fig. 3g, Supplementary Fig. 5b, h), highlighting the crucial roles of CIB2 D90 and D93. Conversely, the CIB2 E11R variant had a modest effect (Fig. 3g, Supplementary Fig. 5c, i). CIB2 Q17A and T20A double mutation led to over a 15-fold decrease in binding affinity (Fig. 3g, Supplementary Fig. 5d, j). For TMC1^{CBD-1}, the K116A variant completely abolished binding (Fig. 3g, Supplementary Fig. 6a, f), the K112E variant significantly reduced binding (Fig. 3g, Supplementary Fig. 6b, g), and the K121E variant had a minor impact (Fig. 3g, Supplementary Fig. 6c, h). Additionally, ITC results showed that both two pairs of the reverse double point mutations (CIB2 D90K-TMC1 K112D and CIB2 D93K-TMC1 K116D) could not restore the binding affinity (Supplementary Fig. 7a–d). Circular dichroism spectroscopy showed that all the four mutations retained well-folded states (Supplementary Fig. 7e, f). Both the M113A variant from TMC1 and the F88Q/V92Q double mutation from CIB2 entirely eradicated the interaction (Fig. 3g, Supplementary Fig. 5e, k, Supplementary Fig. 6d, i), confirming the vital role of hydrophobic interactions in complex formation, in agreement with our previous mapping results (Fig. 1b). The F21Q mutation from CIB2 and K107A mutation from TMC1 variably reduced the interaction as expected (Fig. 3g, Supplementary Fig. 5f, l, Supplementary Fig. 6e, j). Together, these mutagenesis results underscore the pivotal roles of the interface residues observed in the CIB2-TMC1^{CBD-1} crystal structure.

High structural conservation of CIB family proteins across species

Sequence alignment has demonstrated a high degree of conservation among CIB2 proteins across species (Supplementary Fig. 8). Remarkably, essential

Table 1 | Statistics of X-ray Crystallographic Data Collection and Model refinement

Data collection	
Data sets	CIB2-TMC1 (PDB: 8XOQ)
Space group	$P2_1$
Wavelength (Å)	0.9791
Unit Cell Parameters (Å)	a = 32.065, b = 121.849, c = 62.208 α = 90°, β = 91.737°, γ = 90°
Resolution range (Å) No. of reflections	50–2.40 (2.44–2.40) 115387
No. of unique reflections	18424 (946)
Redundancy	6.3 (5.4)
I/σ	15.14 (6.61)
Completeness (%)	99.4(99.5)
R_{merge} [a] (%)	12.4 (26.3)
$CC_{1/2}$ (last resolution shell) [b]	0.948
Structure refinement	
Resolution (Å)	43.55–2.41 (2.47–2.41)
R_{cryst} [c]/R_{free} [d] (%)	20.13/24.22
rmsd bonds (Å) / angles (°)	0.004/1.258
Average B factor (Å^2) [e]	39.57 (CIB2-TMC1) 34.62 (Water) 32.95 (Mg^{2+})
No. of atoms	
Protein atoms	3806
Water	88
Ligands	0
No. of reflections	
Working set	16,584
Test set	908
Ramachandran plot regions [e]	
Favored (%)	98.04
Allowed (%)	1.96
Outliers (%)	0.22

Numbers in parentheses represent the value for the highest resolution shell.
[a]$R_{merge} = \Sigma |I_i - <I>| / \Sigma I_i$, where I_i is the intensity of measured reflection and <I> is the mean intensity of all symmetry-related reflections.
[b]$CC_{1/2}$ were defined by Karplus and Diederichs[46].
[c]$R_{cryst} = \Sigma||F_{calc}| - |F_{obs}|| / \Sigma F_{obs}$, where F_{obs} and F_{calc} are observed and calculated structure factors.
[d]$R_{free} = \Sigma_T ||F_{calc}| - |F_{obs}|| / \Sigma F_{obs}$, where T is a test data set of about 5% of the total unique reflections randomly chosen and set aside prior to refinement.
[e]B factors and Ramachandran plot statistics are calculated using MOLPROBITY[44].

interface residues in the human CIB2-TMC1^{CBD-1} complex are also present in the recently resolved CALM-1-TMC-1 complex of *C. elegans*, as determined by cryo-EM[17]. For instance, residues E11, D90, and D93 from human CIB2 are identical to E23, D104, and D107 from CALM-1 (Fig. 4a, b), playing a crucial role in the CALM-1-TMC-1 interface[17]. Structural alignment of human CIB2 with *C. elegans* CALM-1, based on backbone alpha carbon atoms, revealed a root mean square deviation (RMSD) of approximately 1.1 Å (Fig. 4b), suggesting a highly conserved mode of interaction between CIB proteins and TMC1 throughout evolution, potentially reflecting their essential physiological roles.

A recent study has unveiled a novel CIB binding site in the first cytoplasmic loop between TM domains 2 and 3 of TMC1 with amino acids 298–359, named CBD-2 here (Fig. 1a), and elucidated the structure of the CIB3-TMC1^{CBD-2} complex[15]. From the sequence alignment data, residues E11, Q17, T20, F21, and D93 in CIB2 are entirely identical to those in CIB3 (Fig. 4a, c), underscoring their importance in the CIB-TMC1^{CBD-1} interface. Furthermore, structural analysis revealed even more pronounced conservation between the CIB2 and CIB3 proteins, with an RMSD of only 1.0 Å (Fig. 4c, d). The alignment indicates that TMC1^{CBD-1} interacts with the N-terminal region of CIB2, while TMC1^{CBD-2} can bind to the C-terminal region on the opposite direction simultaneously (Fig. 4d). These observations suggest that the two TMC1 binding sites on CIB2 are distinct and non-overlapping. This conclusion aligns with findings in *C. elegans*, where CALM-1 exhibits similar multifaceted binding characteristics[17,18].

The structural comparison between the cryo-EM complexes of TMC-1 and TMC-2 reveals that the CIB2-TMC1 complex exhibits a high degree of structural conservation with both TMC1 and TMC2 across most regions (Fig. 4e, f). The backbone RMSD values, calculated by aligning 145 Cα atoms corresponding to CIB2 and CALM-1, are 1.19 Å for CIB2-TMC1 versus TMC-1 complex and 1.09 Å for CIB2-TMC1 versus TMC-2 complex, underscoring their conserved architecture. While CIB2 and CALM-1 share significant sequence and structural similarity, distinct spatial arrangements arise upon binding with metal ions. In the CIB2-TMC1 complex, the EF3 and EF4 domains of CIB2 are positioned closer together compared to the corresponding domains of CALM-1 in the TMC-1 and TMC-2 complexes (Fig. 4e, f). This spatial rearrangement leads to a positional shift of approximately 4.5 Å in the TMC1^{CBD-1} region within the CIB2-TMC1 complex relative to its positioning in the TMC-1 and TMC-2 complexes. The binding interfaces of CIB2 and CALM-1 with TMC1^{CBD-1} exhibit near-identity, while the CALM-1–TMC1^{CBD-2} interface shows high similarity to the interface observed in the CIB3-TMC1 complex (Fig. 4d). Both CIB2 and CALM-1 interact with TMC1^{CBD-1} predominatly via the H1–H3 helices of TMC1, which adopt a paddle-like orientation, lying parallel to the membrane and embedding into CIB2 or CALM-1. The interaction between CALM-1 and TMC-1^{CBD-1} relies primarily on electrostatic forces. In contrast, the CIB2–TMC1^{CBD-1} interaction involves electrostatic, hydrophobic, hydrogen-bonding, and cation-π interactions, forming a complex interaction network. Our analysis precisely identified the amino acid pairs involved in each type of interaction. Using site-directed mutagenesis, we further validated the critical residues essential for the formation of the CIB2-TMC1^{CBD-1} complex, providing a detailed interaction mechanism. Additionally, CALM-1 engages TMC1^{CBD-2} via the cytoplasmic H5–H6 helices of TMC-1, predominantly through hydrophobic interactions. This interaction mode is consistent with the CIB3-TMC1 complex, further highlighting the conserved nature of these molecular interactions. These findings underscore both the conserved and species-specific adaptations of the interactions between CIB family proteins and TMC complexes, reflecting their evolutionary significance and mechanistic diversity.

Based on these studies, we next evaluated the binding between full-length TMC1 and CIB2 through co-immunoprecipitation (Co-IP) experiments. Specifically, we co-transfected GFP-tagged full-length TMC1 protein (either wild-type or variants) and 3xFlag-tagged CIB2 into HEK-293T cells. We utilized anti-Flag beads to immunoprecipitate the cell lysates and detected TMC1-GFP signals using GFP antibodies. These experiments were repeated in three independent batches. We observed robust binding when using the full-length wild-type TMC1 protein with CIB2 (Fig. 4g, Supplementary Fig. 9). Conversely, mutations at critical residues, including either TMC1 CBD-1 (M113A, K116A, or M113A and K116A double mutation), TMC1 CBD-2 (F318R, W321D, or F318R and W321D double mutation), or another potential binding region (K175A and E178A double mutation) in the TMC1 full-length protein, congruously dismissed the interaction with CIB2 (Fig. 4g, Supplementary Fig. 9). These results suggest that both TMC1 CBD-1 and TMC1 CBD-2 are crucial for a complete interaction with CIB2 under physiological conditions.

Calcium-dependent modulation of CIB2-TMC1 interactions

Given that CIB2 binds Ca^{2+} and undergoes conformational changes[24,26], we evaluated the capability of Ca^{2+}-bound CIB2 to interact with TMC1 using ITC assays. We observed a progressive enhancement in the CIB2-TMC1^{CBD-1} interaction with escalating concentrations of Ca^{2+} (Fig. 5a, b), in stark contrast to the Ca^{2+}-free condition which exhibited a K_d of approximately 0.3 μM (Fig. 1d). Notably, this enhancement in binding

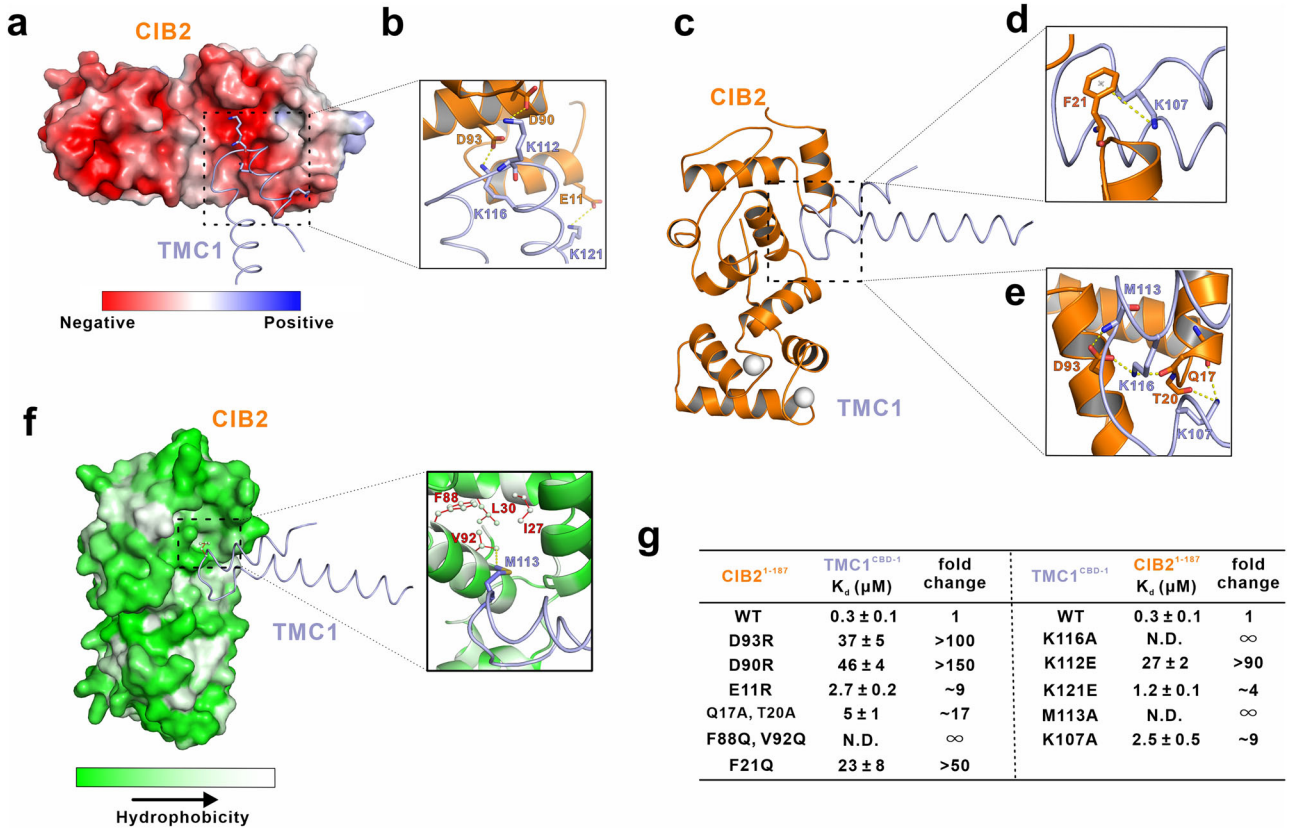

g

$CIB2^{1-187}$	$TMC1^{CBD-1}$ K_d (μM)	fold change	$TMC1^{CBD-1}$	$CIB2^{1-187}$ K_d (μM)	fold change
WT	0.3 ± 0.1	1	WT	0.3 ± 0.1	1
D93R	37 ± 5	>100	K116A	N.D.	∞
D90R	46 ± 4	>150	K112E	27 ± 2	>90
E11R	2.7 ± 0.2	~9	K121E	1.2 ± 0.1	~4
Q17A, T20A	5 ± 1	~17	M113A	N.D.	∞
F88Q, V92Q	N.D.	∞	K107A	2.5 ± 0.5	~9
F21Q	23 ± 8	>50			

Fig. 3 | Detailed molecular interface of the CIB2-TMC1 complex. a Electrostatic potential surface analysis of CIB2 showing a negatively charged central pocket that corresponds to the TMC1 binding site. **b** Ribbon diagram showing the detailed electrostatic interactions between CIB2 and TMC1. In this drawing, the interface highlights the salt bridges between D90 and D93 from CIB2 with K112 and K116 from TMC1, respectively, and a charge-charge interaction between E11 from CIB2 and K121 from TMC1. Residues involved in the binding are shown in stick model. The salt bridges are shown as dotted lines. **c**, **d** Ribbon diagram showing a pair of π-cation interaction between K107 from TMC1 and F21 from CIB2. **e** Ribbon diagram showing the hydrogen bonding interactions between CIB2 and TMC1. In this drawing, the interface highlights several hydrogen bonds including Q17 and T20 from CIB2 with K107 from TMC1, and between D93 from CIB2 and M113 from TMC1. Residues involved in the binding are shown in stick model. The hydrogen bonds are shown as dotted lines. **f** Surface representation of CIB2 colored according to Eisenberg hydrophobicity scale. Ribbon-stick diagram showing that the key residues involved in hydrophobic interactions. CIB2 forms hydrophobic pocket and the side chain of TMC1 M113 is inserted into the hydrophobic pocket on CIB2, composed of I27, L30, F88, and V92, contributing to the complex's stability. **g** The measured binding affinities between various mutations of CIB2 1-187 and $TMC1^{CBD-1}$ based on ITC assays and comparison against CIB2 1-187 WT (wild-type) in binding with $TMC1^{CBD-1}$ (left). The measured binding affinities between various. mutations of $TMC1^{CBD-1}$ and the CIB2 1-187 based on ITC assays and comparison against $TMC1^{CBD-1}$ WT in binding with CIB2 1-187 (right).

affinity plateaued at a Ca^{2+} concentration of 1 mM, with no further increase beyond this concentration, as the affinity remained unchanged at the Ca^{2+} concentration of 3 mM (Fig. 5c). Given the distinct localization of $TMC1^{CBD-1}$ and $TMC1^{CBD-2}$ binding sites on opposing facets of CIB2, we probed whether the binding dynamics differed for the formation of these individual complexes.

In a distinct contrast to the CIB2-$TMC1^{CBD-1}$ interaction, no binding of CIB2 to $TMC1^{CBD-2}$ was observed under Ca^{2+}-free conditions (Fig. 5d, e). We then investigated CIB2-CBD2 interaction with multiple Ca^{2+} concentrations including 10 μM, 40 μM, 100 μM, 300 μM, 0.5 mM, and 3 mM via ITC experiments (Fig. 5d, Supplementary Fig. 10). It exhibited very weak binding between CIB2 and CBD-2 with a K_d over 100 μM with 10 μM or 40 μM Ca^{2+} (Supplementary Fig. 10a–b). Upon increasing the Ca^{2+} concentration to 100 μM, a strong interaction was noted (Supplementary Fig. 10c). Additionally, the ITC results showed an enhancement in the interaction between CIB2 and $TMC1^{CBD-2}$ when the Ca^{2+} concentration increased from 300 μM to 3 mM (Supplementary Fig. 10d–f). Specifically, CIB2 exhibited a markedly high-affinity binding to $TMC1^{CBD-2}$ with a K_d of approximately 0.4 μM when the Ca^{2+} concentration is 0.5 mM (Fig. 5d, Supplementary Fig. 10e). We further investigated whether Ca^{2+}-bound CIB2 could simultaneously interact with both $TMC1^{CBD-1}$ and $TMC1^{CBD-2}$. A mixture of CIB2 with equimolar concentrations of $TMC1^{CBD-1}$ and $TMC1^{CBD-2}$ (70 μM each) in 0.5 mM Ca^{2+} resulted in the formation of a ternary complex, as evidenced by a new peak (red line) in the chromatography distinct from those individual 1:1 complex of CIB2 with either $TMC1^{CBD-1}$ or $TMC1^{CBD-2}$ (Fig. 5g). To ascertain the calcium dependency of these interactions, we employed a CIB2 double mutant (D127A/D168A) with impaired Ca^{2+} binding (Fig. 5h). This mutant displayed an inability to bind $TMC1^{CBD-2}$ in the presence of 3 mM Ca^{2+} (Fig. 5i), and exhibited a reduced affinity for $TMC1^{CBD-1}$ (Fig. 5j). These findings collectively underscore the criticality of Ca^{2+} in facilitating CIB2's simultaneous engagement with both $TMC1^{CBD-1}$ and $TMC1^{CBD-2}$, highlighting the pivotal role of calcium in the molecular interaction dynamics of these proteins.

The CBD-1 and CBD-2 domains of hTMC1 display a significant degree of similarity to the corresponding amino acid sequences of hTMC2 CBD-1 (aa 150-200) and hTMC2 CBD-2 (aa 363-424) (Supplementary Fig. 11a). CIB2 also binds to $TMC2^{CBD-1}$ with a K_d of approximately 0.6 μM in 0.5 mM Ca^{2+}, showing a slightly stronger affinity compared to Ca^{2+}-free condition (Supplementary Fig. 11b–c). $TMC2^{CBD-2}$ showed weak interaction with CIB2 without Ca^{2+} (Supplementary Fig. 11d), and exhibited higher binding affinity to CIB2 in 0.5 mM Ca^{2+} (Supplementary Fig. 11e). Collectively, these findings demonstrated the Ca^{2+} regulation of CIB2's interaction with both $TMC2^{CBD-1}$ and $TMC2^{CBD-2}$.

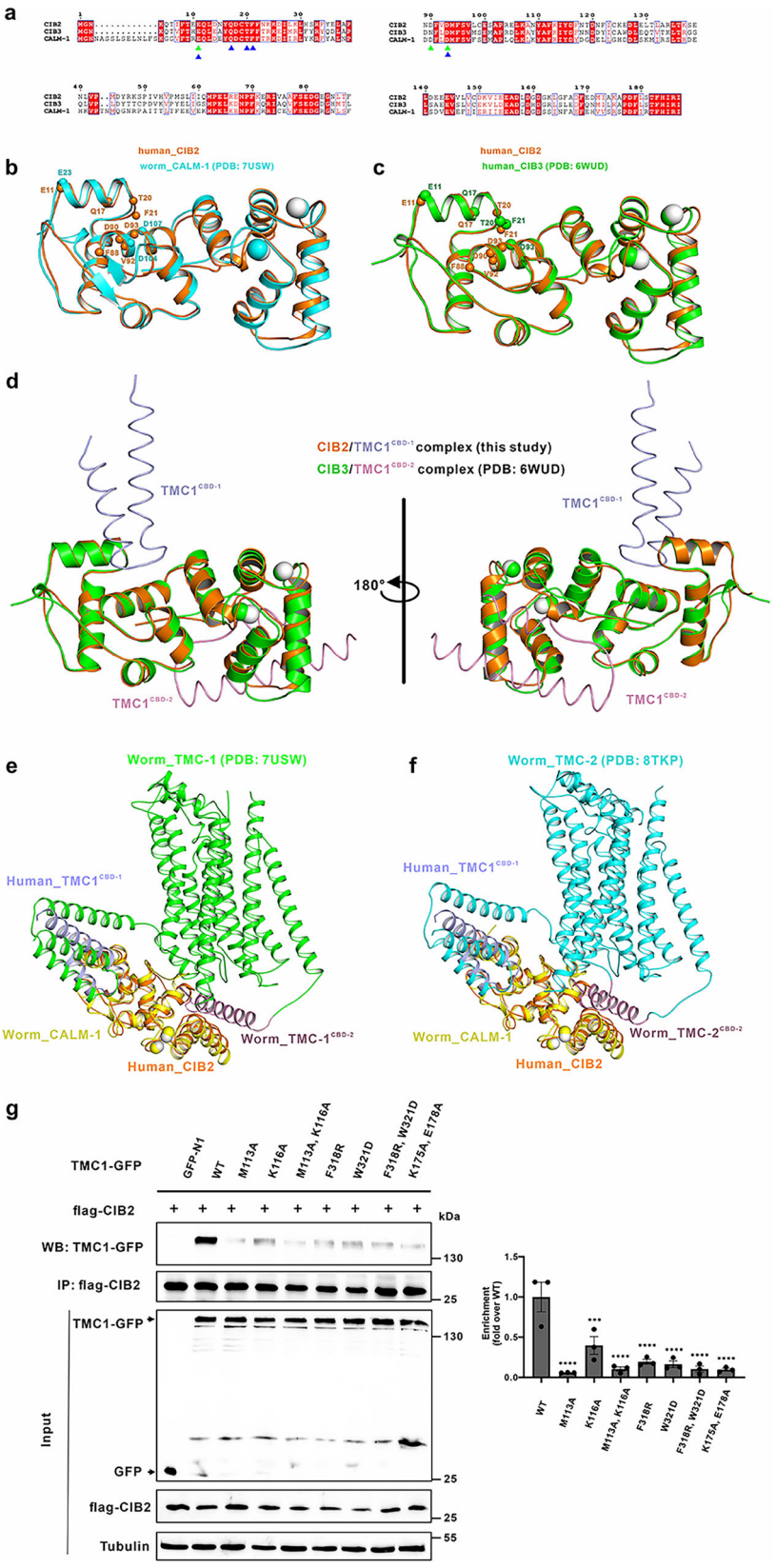

Fig. 4 | The CIB family exhibits a high degree of structural conservation. a Sequence alignment of human CIB2, human CIB3, and *C. elegans* CALM-1. Residues that are identical and highly similar are indicated in red and transparent boxes, respectively. The location of key residues for TMC1^{CBD-1} binding are indicated on the sequence. E23, D104, and D107 from CALM-1 are labeled with green triangles while E11, Q17, T20, F21, and D93 from CIB3 are labeled with blue triangles. Those residues play crucial roles in the CALM-1-TMC-1 interface or CIB3-TMC-1 interface. **b** Superposition of CIB2 (orange) and CALM-1 (cyan, PDB: 7USW) using backbone α -carbon atoms highlights structural conservation (RMSD = 1.1 Å). Calcium ions from CALM-1 structure are shown as cyan spheres and magnesium ions from CIB2 structure are shown as gray spheres. CIB2 residues for TMC1^{CBD-1} binding are shown as orange spheres, CALM-1 residues for TMC1 H1-H3 binding are shown as cyan spheres. **c** Superposition of CIB2 (orange) and CIB3 (green, PDB: 6WUD) using backbone α -carbon atoms highlights structural conservation (RMSD = 1.0 Å). Magnesium ions from CIB3 structure are shown as green spheres while magnesium ions from CIB2 structure are shown as gray spheres. CIB2 residues for TMC1^{CBD-1} binding are shown as orange spheres, CIB3 residues that conserved with CIB2 are shown as green spheres. **d** Structure alignment of CIB2-TMC1^{CBD-1} complex and CIB3-TMC1^{CBD-2} (PDB: 6WUD) complex. CIB2 is shown in orange, and TMC1^{CBD-1} is shown in light blue. CIB3 is shown in green, and TMC1^{CBD-2} is shown in pink. Magnesium ions from CIB3 structure are shown as green spheres and magnesium ions from CIB2 structure are shown as gray spheres. **e** Structure alignment of CIB2-TMC1^{CBD-1} complex and TMC-1 complex (PDB 7USW). CIB2 is shown in orange, TMC1^{CBD-1} in light blue, TMC-1 in green, and TMC1^{CBD-2} in pink. CALM-1 is displayed in yellow. Calcium ions from the CALM-1 structure are represented as yellow spheres, and magnesium ions from the CIB2 structure are shown as gray spheres. **f** Structure alignment of CIB2-TMC1^{CBD-1} complex and TMC-2 complex (PDB 8TKP). CIB2 is shown in orange, TMC1^{CBD-1} in light blue, TMC-2 in cyan, TMC-2^{CBD-2} in pink. CALM-1 is displayed in yellow. Calcium ions from the CALM-1 structure are represented as yellow spheres, and magnesium ions from the CIB2 structure are shown as gray spheres. **g** Co-IP analysis of the binding between full-length TMC1 and CIB2. HEK-293T cells co-expressing TMC1-GFP WT or TMC1-GFP variants and CIB2 followed by anti-Flag beads to immunoprecipitate and detected using GFP antibodies. Data are represented as the mean ± SEM ($n = 3$). ***$p < 0.001$; ****$p < 0.0001$ based on one-way ANOVA with Dunnett's test.

Deafness-related CIB2 mutations variably affect TMC1^{CBD-1} and TMC1^{CBD-2} binding

In light of the divergent binding specificities of CIB2 for TMC1^{CBD-1} and TMC1^{CBD-2}, we further explored whether mutations in CIB2 associated with deafness variably influence its affinity for these two sites. We examined seven CIB2 mutations implicated in hearing loss, including E64D, R66W, F91S, C99W, Y115C, I123T, and R186W[10,27,28] (Fig. 6a), which are conserved across human CIB2, human CIB3, and CIB2 orthologs (Supplementary Fig. 1b, Fig. 8). Notably, none of these mutations was located at the identified interfaces with TMC1^{CBD-1} and TMC1^{CBD-2}.

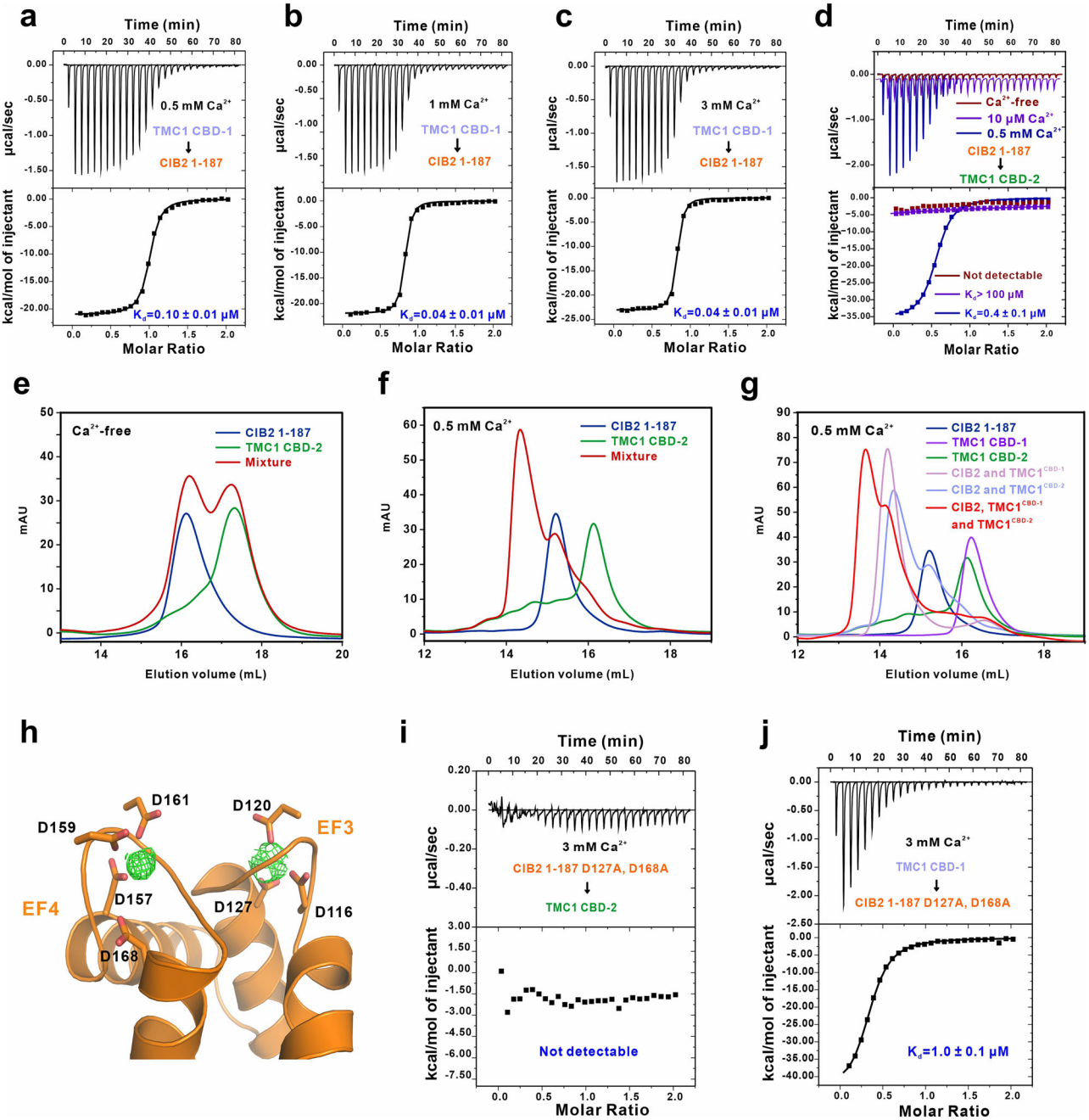

Fig. 5 | Calcium-dependent modulation of CIB2-TMC1 interactions. a–c ITC based measurements of the binding affinities between CIB2 1-187 and $TMC1^{CBD-1}$ under different calcium concentrations, including 0.5 mM Ca^{2+} (**a**) 1 mM Ca^{2+} (**b**) and 3 mM Ca^{2+} (**c**) showing Ca^{2+} elevates the interaction between CIB2 and $TMC1^{CBD-1}$. **d** ITC-derived binding curves comparing the binding affinities between CIB2 1-187 and $TMC1^{CBD-2}$ complex under the condition of Ca^{2+} free (dark red) or 10 µM Ca^{2+} (purple) or 0.5 mM Ca^{2+} (blue), showing Ca^{2+} is absolutely required for CIB2-$TMC1^{CBD-2}$ interaction. **e** AGFC experiment revealed that no interaction is detected between CIB2 1-187 and $TMC1^{CBD-2}$ in Ca^{2+} free condition. **f** AGFC experiment indicated that direct interaction exists between CIB2 1-187 and $TMC1^{CBD-2}$ in 0.5 mM Ca^{2+} buffer condition. **g** AGFC experiments demonstrated that CIB2 1-187 could simultaneously interact with both $TMC1^{CBD-1}$ and $TMC1^{CBD-2}$ in 0.5 mM Ca^{2+}. **h** Bijvoet difference map density, in green mesh, shows a lack of cation occupancy in EF hands 3 and 4. The D116, D120, D127, D157, D159, D161, and D168 side chains are labeled and represented in sticks. **i**, **j** ITC based measurements of the binding affinities between EF-hand double mutations of CIB2 1-187 and $TMC1^{CBD-2}$ in 3 mM Ca^{2+} (**i**) and $TMC1^{CBD-1}$ in 3 mM Ca^{2+} (**j**).

However, pull-down assays revealed a pronounced impact of these mutations on both $TMC1^{CBD-1}$ and $TMC1^{CBD-2}$ bindings. In particular, the F91S mutation in CIB2 almost entirely negated binding to $TMC1^{CBD-1}$, while the C99W mutation significantly impaired $TMC1^{CBD-1}$ binding, albeit to a lesser extent for other variants (Fig. 6b). Structurally, residue F91 in CIB2, situated proximal to the binding interface, engages in hydrophobic interactions with F34 and F95 (Fig. 6c). The substitution of F91 with serine, a hydrophilic residue, presumably disrupts the hydrophobic environment, consequently destabilizing CIB2's conformation and diminishing its affinity for $TMC1^{CBD-1}$.

In contrast, the I123T mutation, which had little effect on $TMC1^{CBD-1}$ binding, substantially hindered $TMC1^{CBD-2}$ binding in the presence of 0.5 mM Ca^{2+} (Fig. 6d). Other mutations, including E64D, C99W, and Y115C also significantly reduced CIB2's binding to $TMC1^{CBD-2}$ (Fig. 6d). R66W and R186W mutations exhibited lesser impacts on both $TMC1^{CBD-1}$ and $TMC1^{CBD-2}$ binding (Fig. 6b, d). In the CIB2 structure, the residue I123,

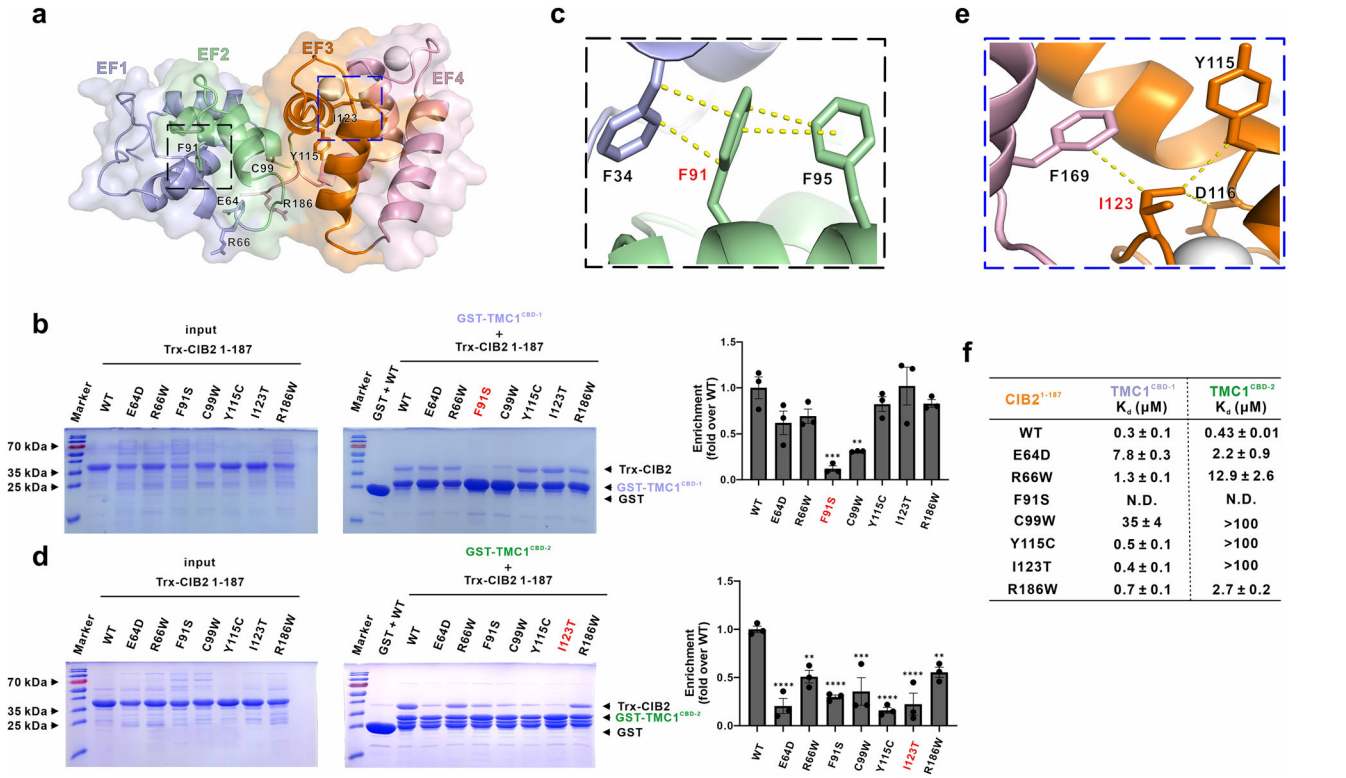

CIB2$^{1-187}$	TMC1^{CBD-1} K_d (μM)	TMC1^{CBD-2} K_d (μM)
WT	0.3 ± 0.1	0.43 ± 0.01
E64D	7.8 ± 0.3	2.2 ± 0.9
R66W	1.3 ± 0.1	12.9 ± 2.6
F91S	N.D.	N.D.
C99W	35 ± 4	>100
Y115C	0.5 ± 0.1	>100
I123T	0.4 ± 0.1	>100
R186W	0.7 ± 0.1	2.7 ± 0.2

Fig. 6 | CIB2 mutations linked to deafness have differential effects on its binding to TMC1^{CBD-1} and TMC1^{CBD-2}. **a** Structural properties of CIB2 and its pathogenetic variants are shown. Cartoon and surface representation are superposed. The N-terminal region and EF1 is colored light blue. EF2, and EF3 are colored green and orange, and the C-terminal region and EF4 is colored pink. Residues affected by pathogenic missense mutations are colored according to the EF-hand domain in which they are located, and magnesium ions are represented by gray spheres. The area where F91 is located is marked with a black border and the area where I123 is located is marked with a blue border. **b** GST pull-down assays showed that the F91S and C99W variants of CIB2 significantly decrease the binding with GST-TMC1^{CBD-1}. Data are represented as the mean ± SEM ($n = 3$). $^{**}p < 0.01$; $^{***}p < 0.001$ based on one-way ANOVA with Dunnett's test. **c** The CIB2 structure model highlights residue F91, which forms hydrophobic interactions and π-π interactions with residues F34 (light blue) and F95 (green). **d** GST pull-down assays showing that the all the variants of CIB2 decrease the binding with GST-TMC1^{CBD-2}. Data are represented as the mean ± SEM ($n = 3$). $^{***}p < 0.001$; $^{****}p < 0.0001$ based on one-way ANOVA with Dunnett's test. **e** The CIB2 structure model highlights residue I123, which forms hydrophobic interactions with residues Y115 (orange) and F169 (pink) and the main chain of D116 (orange). **f** ITC-based measurements of the binding affinities of CBD-1 or CBD-2 and various CIB2 deafness-related mutants including E64D, R66W, F91S, C99W, Y115C, I123T, and R186W.

located within the EF3 loop, forms robust hydrophobic interactions with F169 and Y115, further stabilized by the mainchain of D116 (Fig. 6e). The introduction of a hydrophilic threonine at this position likely disrupts this hydrophobic milieu. Such a conformational shift could potentially alter the orientation of EF3 calcium ligands, thereby diminishing calcium affinity and, by extension, TMC1^{CBD-2} binding. A similar mechanism underlies the compromised TMC1^{CBD-2} binding observed with the Y115C mutant. These findings provide a molecular basis for previous observations that the F91S and I123T mutations in CIB2 markedly reduce TMC1/2 binding and impair mechanotransduction[15]. Furthermore, the results obtained from ITC experiments are consistent with those derived from the pull-down assays (Fig. 6f, Supplementary Fig. 12, Supplementary Fig. 13). CD results showed that most of the mutants retain the typical helical folding, but the folding of the F91S mutant appears to be somewhat affected (Supplementary Fig. 14).

In summary, our study demonstrates that specific mutations linked to deafness in CIB2 can differentially disrupt its binding to TMC1^{CBD-1} (notably F91S) or TMC1^{CBD-2} (predominantly I123T). Several of these mutations, such as I123T and Y115C, appear to adversely affect TMC1^{CBD-2} binding through impaired calcium sensing capability (Fig. 6e).

Discussion

The mechanoelectrical transduction (MET) channel complex in the stereocilia of mammalian hair cells plays a pivotal role in auditory perception. However, the molecular interactions between the TMC1 and its critical auxiliary subunits CIB2/CIB3 remain largely unexplored. In this study, we elucidated the CIB2-TMC1 interaction by resolving the structure of the CIB2-TMC1^{CBD-1} complex and pinpointing essential interface residues. Significantly, this interaction is modulated by calcium, evidenced by the increased affinity of Ca^{2+}-bound CIB2 for TMC1^{CBD-1}, while the binding between CIB2 and TMC1^{CBD-2} is totally calcium-dependent. Consequently, CIB2 can simultaneously interact with both the TMC1^{CBD-1} and TMC1^{CBD-2} sites on TMC1 in the presence of Ca^{2+}. We also discovered that certain mutations in CIB2 linked to deafness variably impair or completely disrupt these interactions, presumably due to disrupting the calcium-binding site on EF hand 3. These finding underscore the critical role of Ca^{2+} in regulating the assembly and functionality of the MET complex.

The interaction mechanisms of CIB2 with TMC1 bear resemblance to the interaction between calmodulin (CaM) and calcium channels, where CaM serves as a classic calcium-sensing protein modulating various ion channels[29,30]. Our findings indicate that TMC1 contains two CIB2 binding sites. At baseline calcium levels, apo-CIB2 binds to TMC1^{CBD-1}. However, with increased Ca^{2+} levels, Ca^{2+}-CIB2 binds to the opposite side CBD-2, effectively linking both TMC1's CBD-1 and CBD-2 domains. This mechanism parallels the dual CaM binding domains in L-type voltage-gated Cav1.2 and Cav1.3 channels, located in the C-terminal IQ-motif and the N-terminal NSCaTE. Under resting conditions, apo-CaM attaches to the IQ-motif. Channel activation and subsequent Ca^{2+} influx leads to Ca^{2+}-CaM binding to NSCaTE, triggering a conformational change that shuts the Cav channel, thus regulating further Ca^{2+} entry[31,32]. Given these analogous binding properties, we propose that Ca^{2+}-CIB2 may similarly induce a

conformational shift in TMC1, resulting in channel closure and inactivation of the MET complex. Several related structures have been determined by cryo-EM and deepen the understanding of CIB-TMC MET complex[17,18]. The structural analysis reveals the proximity of the CALM-1 Ca^{2+} binding sites to the interface between CALM-1 and TMC-1 in *C. elegans*, thereby highlighting the roles of both Ca^{2+} and CALM-1 in shaping the conformation of TMC-1[17]. While TMC-1 or TMC-2 MET complexes exhibit a closed putative ion-conduction pathway, its open conformation remains unidentified.

In resting conditions, MET channels in cochlear hair cells are not fully closed, allowing a baseline influx of Ca^{2+} even without auditory stimuli[33–35]. This state sets the channel's position along the activation curve, priming it for maximum sensitivity to mechanical stimulation. The opening probability (Po) of transduction channels at rest is influenced by external and internal Ca^{2+} concentrations[36,37]. Supporting our hypothesis, recent study show that the resting Po in OHCs from $Tmc1^{dn/dn}$;$Cib2^{R186W/+}$ mutants is higher in high BAPTA concentrations, with MET currents significantly reduced at negative potentials when external Ca^{2+} levels are increased[15]. Additionally, the structure of the TMC1 complex from *C. elegans* in the presence of Ca^{2+}-loaded CALM-1 reveals a closed conformation[17], further substantiating our hypothesis.

Calcium sensor proteins play a vital role in modulating ion channel functions through calcium-mediated interactions. For instance, the neuronal calcium sensor KChIPs interact with the N-terminus of Kv4 potassium channels, influencing their gating, surface expression, and assembly[38]. Notably, KChIP1 variants incapable of calcium binding do not significantly alter the amplitude or kinetics of Kv4.3 currents compared to native KChIP1[39]. In the realm of photoreceptors, cyclic nucleotide-gated (CNG) channels exhibit optimal open probability at lower calcium concentrations[40]. The binding of Ca^{2+}-calmodulin to CNGB1 is instrumental in the calcium-dependent desensitization of retinal rod CNG channels, a process crucial for light adaptation. Disturbances in this calcium-dependent mechanism of CNG channel function are linked to inherited blindness[41]. These instances underscore the fundamental role of calcium sensor proteins, akin to CIB2, in orchestrating ion channel function via calcium-centric interactions.

Numerous deafness-linked CIB2 mutations have been identified[27], but their impact on CIB2 binding to $TMC1^{CBD-1}$ and $TMC1^{CBD-2}$ are unclear. Our investigation of seven CIB2 mutants revealed that two mutations (F91S, C99W) significantly impair CIB2-$TMC1^{CBD-1}$ binding, while four others (E64D, C99W, Y115C, I123T) notably reduce CIB2-$TMC1^{CBD-2}$ binding (Fig. 6). The Y115C and I123T mutations likely alter the structure of CIB2's EF-hand 3, diminishing its calcium-binding capacity. Additionally, the E64D mutant shows decreased calcium affinity and fails to attain a native conformation even at high calcium levels[24]. Our research indicates that numerous mutations linked to deafness compromise calcium binding in CIB2, suggesting that calcium-dependent CIB2-TMC1 interactions are essential for auditory function. This breakthrough offers promising avenues for developing therapeutic strategies aimed at rectifying calcium-binding anomalies associated with CIB2-related deafness.

While further investigation is needed to fully understand the calcium-dependent effects on the MET channel, our findings lay the groundwork for the molecular and structural understanding of CIB2-$TMC1^{CBD-1}$ complex formation. They also highlight the significant role of calcium in the assembly of the MET channel. Future functional studies focusing on calcium-bound CIB2 are crucial to determine whether CIB2 influences the mechanotransduction process.

Materials and Methods

Constructs, protein expression and purification

The coding sequences of the human CIB2 (UniProt: O7538), mouse CIB3 (UniProt: A0A5F8MPX9), and human $TMC1^{CBD-1}$ or $TMC1^{CBD-2}$ (UniProt: Q8TDI8) constructs were PCR amplified from cDNA libraries. The mouse CIB1 (UniProt: Q9Z0F4) and mouse CIB4 (UniProt: Q9D9N5) constructs were generous gifts from Dr. Qing Lu (Shanghai Jiaotong University). The GFP-N1 tagged full-length human TMC1 constructs were generous gifts from Dr. Yiquan Tang (Fudan University). All of the protein constructs were cloned into a modified pET32a vector for protein expression and confirmed by DNA sequencing. The fusion constructs used for crystal screening were made by two-step PCR with a linker sequence of "GSLVPRGS" between TMC1 and CIB2. In particular, the consult for solving the crystal structure is made through fusing the $TMC1^{CBD-1}$ (residues 86–136) at the N-terminal of CIB2 full-length (residues 1–187) with the above linker sequence. The various mutations or short fragments of CIB2 and TMC1 were generated by standard PCR-based methods and confirmed by DNA sequencing. All the proteins were expressed in *Escherichia coli* BL21 (DE3) cells. The N-terminal thioredxin-His_6-tagged proteins were purified using Ni-NTA agarose affinity column followed by size-exclusion chromatography (Superdex 200 column, GE Healthcare) in the buffer containing 50 mM Tris (pH 7.8), 100 mM NaCl, 1 mM DTT, and either 1 mM EDTA, or 0.5/1/3 mM $CaCl_2$. For crystal screening proteins, the thioredxin-His_6 tag was removed by incubation with HRV 3 C protease at 4 °C overnight and separated by size-exclusion chromatography.

Isothermal titration calorimetry assay

Isothermal titration calorimetry (ITC) measurements were carried out on a VP-ITC MicroCal calorimeter (Malvern) at 25 °C. All proteins were dissolved in the buffer containing 50 mM Tris (pH 7.8), 100 mM NaCl, 1 mM DTT, and either 1 mM EDTA, or 0.5/1/3 mM $CaCl_2$. TMC1 proteins (200 μM) were loaded into the syringe, and CIB2 proteins (20 μM) were loaded in the cell. Each titration point was performed by injecting a 10 μl aliquot of syringe protein into the cell at a time interval of 180 s to ensure that the titration peak returned to the baseline. The titration data were analyzed using the program Origin 7.0 (MicroCal) and fitted by the one-site binding model. All the ITC experiments have been repeated more than twice.

AGFC assay

Analytical gel filtration chromatography was carried out on an AKTA Pure system (GE Healthcare). Recombinant proteins with N-terminal His6-tag were concentrated to 70 μM and loaded onto a Superdex200 increase 10/300 GL column (GE Healthcare) equilibrated with the assay buffer (50 mM Tris (pH 7.8), 100 mM NaCl, 1 mM DTT, and either 1 mM EDTA, or 0.5 mM $CaCl_2$.). All the graphs here were drawn by GraphPad Prism 5.

AGFC coupled with static light scattering

The analysis was performed on an AKTA Pure system (GE Healthcare) coupled with a static light scattering detector (miniDawn, Wyatt) and a differential refractive index detector (Optilab, Wyatt). Protein samples (concentration of 70 μM for CIB2 and TMC1) were filtered and loaded into a Superdex 200 increase column. Data were analyzed with ASTRA7 (Wyatt).

GST pull-down assay

For GST pull-down assays, GST-tagged $TMC1^{CBD-1}$ protein was purified in the buffer containing 50 mM Tris, 100 mM NaCl, 1 mM EDTA, and 1 mM DTT at pH 7.8, and GST-tagged $TMC1^{CBD-2}$ was purified in the buffer containing 50 mM Tris, 100 mM NaCl, 0.5 mM $CaCl_2$, and 1 mM DTT at pH 7.8, detected by SDS-PAGE and Coomassie blue staining. The purified CIB2 mutant proteins (E64D, R66W, F91S, C99W, Y115C, I123T, R186W) (60 μM) were incubated with 20 μM of distinct GST, GST-$TMC1^{CBD-1}$, or GST-$TMC1^{CBD-2}$ for 2 h at 4 °C. The 30 μL GSH-sepharose 4B slurry beads in the protein purification buffer were then incubated with the protein mixture for 1 h at 4 °C. After three times wash with the protein purification buffer, the captured proteins were eluted by 20 μl SDS-PAGE loading dye and detected by coomassie blue staining in the SDS-PAGE gels. These experiments were repeated in three independent batches.

Co-immunoprecipitation and western blotting

HEK-293T cells were transfected with plasmids using polyethylenimine (PEI). 48 hours post-transfection, cells were washed with fresh PBS and lysed using RIPA buffer containing 150 mM NaCl, 50 mM Tris (pH 7.4), 1% Triton X-100, 1% Sodium Deoxycholate, 0.1% Sodium Dodecyl Sulfate (SDS) and a protease inhibitor cocktail. The lysates were then rotated for 30 min at 4 °C, followed by centrifugation at 14,000 rpm for 30 min at 4 °C.

Subsequently, 10% of the lysate was reserved as an input control. The remaining lysate underwent overnight immunoprecipitation at 4 °C using 20 µL of anti-DYKDDDDK Affinity Beads (Smart Lifesciences Cat# SA042001). Post-immunoprecipitation, the beads were washed three times with 1x PBST (1x PBS with 0.1% Tween-20). Immunoprecipitated proteins were then eluted using 2x SDS-PAGE sample loading buffer and resolved on SDS-PAGE before being transferred to PVDF membranes (Sigma). These membranes were blocked for 1 hour with 5% skim milk powder in 1x PBST, then incubated overnight at 4 °C with primary antibodies (1:1000 dilution each for mouse anti-GFP (Proteintech, Cat# 66002-1-Ig), mouse anti-FLAG (Proteintech, 66008-4-Ig), or rabbit anti-α-tubulin(Proteintech, 11224-1-AP)). Following primary antibody incubation, the membranes were washed three times with 1x PBST and incubated for 1 hour at room temperature with secondary antibodies (1:10000 for goat anti-mouse IgG-HRP (Absin, Abs20001) or goat anti-rabbit IgG-HRP(Absin, Abs20002)) diluted in 5% milk in 1x PBST. After three additional PBST washes, the membranes were developed using BeyoECL (Beyotime) and imaged on a Tanon 5200 system.

Circular Dichroism measurements

The CD spectra of the proteins were acquired on a JASCO J-1700 CD Spectrometer at the room temperature using a cell path length of 0.5 mm. Each spectrum was collected with three scans spanning a spectral window of 190–260 nm. CIB2 WT and mutant proteins (E64D, R66W, F91S, C99W, Y115C, I123T, and R186W) were purified and diluted into 0.2 mg/mL in a buffer containing 25 mM Tris pH 7.8, 50 mM NaCl, 0.5 mM EDTA and 0.5 mM DTT.

Protein crystallization and structure determination

Crystals of the CIB2-TMC1 complex were obtained by the hanging drop vapor diffusion method at 16 °C under the condition of 25% (w/v) Polyethylene glycol 3350, 0.1 M Tris (pH 8.5), 0.2 M Magnesium chloride hexahydrate. 25% glycerol was added as the cryo-protectant before diffraction data collection. The diffraction data were collected at Shanghai Synchrotron Radiation Facility and processed using HKL2000. The structure was solved by PHASER software[42] using molecular replacement method with the structure of CIB3 (PDB: 6WU5) as the search model. The model of TMC1 was manually built according to the difference electron-density map in COOT[43]. Further model modifications and refinements were repeated alternatively using COOT software and PHENIX software. The final model was validated using MolProbity[44] and the statistics are shown in Table 1. The structure figures were made using PyMol software (https://www.pymol.org).

Sequence alignment analysis

The sequence of the human CIB2 and human TMC1/2 protein was obtained from the UniProt database, and this sequence was submitted to the NCBI-BLAST to search for homologs. CIB and TMC homologous sequences were selected and aligned using multiple sequence alignment (https://www.genome.jp/tools-bin/clustalw) with default parameters. The ESpript 3.0 software was used to generate the color-coded version of the multiple sequence alignment (http://espript.ibcp.fr/ESPript/cgi-bin/ESPript.cgit). Phylogenetic tree of CIB1-4 was made by the software of MEGA11[45].

Statistics and reproducibility

For both the pull-down and co-immunoprecipitation (Co-IP) analyses, we performed at least three independent experiments. Data were statistically analyzed using one-way ANOVA with Dunnett's test to compare test samples to the control, and results are presented as mean ± SEM. The threshold for statistical significance was set at $p < 0.05$ for all tests. Data analysis was conducted using ImageJ and GraphPad Prism version 9.5.0. Source data are included with this paper.

Reporting summary

Further information on research design is available in the Nature Portfolio Reporting Summary linked to this article.

Data availability

All data needed to evaluate the conclusions in the paper are present in the paper and/or the Supplementary information. Source data for the figures can be found in the Supplementary Data 1. The atomic coordinates of the CIB2-TMC1 complex have been deposited to the Protein Data Bank under the accession code: 8XOQ.

Received: 5 June 2024; Accepted: 17 February 2025;
Published online: 25 February 2025

References

1. Tilney, L. G., Tilney, M. S. & DeRosier, D. J. Actin Filaments, Stereocilia, and Hair Cells: How Cells Count and Measure. *Annu. Rev. Cell Biol.* **8**, 257–274 (1992).
2. Pan, B. et al. TMC1 and TMC2 Are Components of the Mechanotransduction Channel in Hair Cells of the Mammalian Inner Ear. *Neuron* **79**, 504–515 (2013).
3. Kurima, K. et al. TMC1 and TMC2 Localize at the Site of Mechanotransduction in Mammalian Inner Ear Hair Cell Stereocilia. *Cell Rep.* **12**, 1606–1617 (2015).
4. Pan, X. Q. & Yan, Z. Q. Discovery of Touch Receptor NOMPC and Hearing Receptor TMC. *Prog. Biochem. Biophys.***48**, 1398–1403 (2021).
5. Fettiplace, R. & Kim, K. X. The physiology of mechanoelectrical transduction channels in hearing. *Physiol. Rev.* **94**, 951–986 (2014).
6. Pan, B. et al. TMC1 Forms the Pore of Mechanosensory Transduction Channels in Vertebrate Inner Ear Hair Cells. *Neuron* **99**, 736–753.e736 (2018).
7. Jia, Y. et al. TMC1 and TMC2 Proteins Are Pore-Forming Subunits of Mechanosensitive Ion Channels. *Neuron* **105**, 310 (2020).
8. Beurg, M., Barlow, A., Furness, D. N. & Fettiplace, R. A Tmc1 mutation reduces calcium permeability and expression of mechanoelectrical transduction channels in cochlear hair cells. *Proc. Natl. Acad. Sci.* **116**, 20743–20749 (2019).
9. Giese, A. P. J. et al. CIB2 interacts with TMC1 and TMC2 and is essential for mechanotransduction in auditory hair cells. *Nat. Commun.* **8**, 43 (2017).
10. Riazuddin, S. et al. Alterations of the CIB2 calcium- and integrin-binding protein cause Usher syndrome type 1J and nonsyndromic deafness DFNB48. *Nat. Genet.* **44**, 1265–1271 (2012).
11. Dal Cortivo, G. et al. Oligomeric state, hydrodynamic properties and target recognition of human Calcium and Integrin Binding protein 2 (CIB2). *Sci. Rep.* **9**, 15058 (2019).
12. Tang, Y.-Q. et al. Ankyrin Is An Intracellular Tether for TMC Mechanotransduction Channels. *Neuron* **107**, 112 (2020).
13. Giese, A. P. J., et al. Complexes of vertebrate TMC1/2 and CIB2/3 proteins form hair-cell mechanotransduction cation channels. bioRxiv, 2023.2005.2026.542533. https://doi.org/10.1101/2023.05.26.542533. (2024).
14. Dal Cortivo, G. & Dell'Orco, D. Calcium- and Integrin-Binding Protein 2 (CIB2) in Physiology and Disease: Bright and Dark Sides. *Int. J. Mol. Sci.* **23**, 3552 (2022).
15. Liang, X. et al. CIB2 and CIB3 are auxiliary subunits of the mechanotransduction channel of hair cells. *Neuron* **109**, 2131–2149.e2115 (2021).
16. Lee, J. H. et al. The Piezo channel is a mechano-sensitive complex component in the mammalian inner ear hair cell. *Nat. Commun.* **15**, 526 (2024).
17. Jeong, H. et al. Structures of the TMC-1 complex illuminate mechanosensory transduction. *Nature* **610**, 796–803 (2022).
18. Clark, S., Jeong, H., Posert, R., Goehring, A. & Gouaux, E. The structure of the Caenorhabditis elegans TMC-2 complex suggests roles of lipid-mediated subunit contacts in mechanosensory transduction. *Proc. Natl. Acad. Sci. USA* **121**, e2314096121 (2024).

19. Wang, X., Li, G., Liu, J., Liu, J. & Xu, X. Z. S. TMC-1 Mediates Alkaline Sensation in C. elegans through Nociceptive Neurons. *Neuron* **91**, 146–154 (2016).
20. Yue, X. et al. TMC Proteins Modulate Egg Laying and Membrane Excitability through a Background Leak Conductance in&IT C. elegans&IT. *Neuron* **97**, 571 (2018).
21. Gentry, H. R. et al. Structural and biochemical characterization of CIB1 delineates a new family of EF-hand-containing proteins. *J. Biol. Chem.* **280**, 8407–8415 (2005).
22. Lepšík, M. & Field, M. J. Binding of Calcium and Other Metal Ions to the EF-Hand Loops of Calmodulin Studied by Quantum Chemical Calculations and Molecular Dynamics Simulations. *J. Phys. Chem. B* **111**, 10012–10022 (2007).
23. Tang, S. & Yang, J. J. Magnesium Binding Sites in Proteins. In Encyclopedia of Metalloproteins, R. H. Kretsinger, V. N. Uversky, and E. A. Permyakov, eds. (Springer New York), pp. 1243–1250. https://doi.org/10.1007/978-1-4614-1533-6_257 (2013).
24. Vallone, R., Dal Cortivo, G., D'Onofrio, M. & Dell'Orco, D. Preferential Binding of Mg2+ Over Ca2+ to CIB2 Triggers an Allosteric Switch Impaired in Usher Syndrome Type 1J. *Front. Mol. Neurosci.* **11**, 274 (2018).
25. Grabarek, Z. Insights into modulation of calcium signaling by magnesium in calmodulin, troponin C and related EF-hand proteins. *Biochimica et. Biophysica Acta (BBA) - Mol. Cell Res.* **1813**, 913–921 (2011).
26. Blazejczyk, M. et al. Biochemical characterization and expression analysis of a novel EF-hand Ca2+ binding protein calmyrin2 (Cib2) in brain indicates its function in NMDA receptor mediated Ca2+ signaling. *Arch. Biochem Biophys.* **487**, 66–78 (2009).
27. Booth, K. T. et al. Variants in CIB2 cause DFNB48 and not USH1J. *Clin. Genet.* **93**, 812–821 (2018).
28. Patel, K. et al. A Novel C-Terminal CIB2 (Calcium and Integrin Binding Protein 2) Mutation Associated with Non-Syndromic Hearing Loss in a Hispanic Family. *PLOS ONE* **10**, e0133082 (2015).
29. Kovalevskaya, N. V. et al. Structural analysis of calmodulin binding to ion channels demonstrates the role of its plasticity in regulation. *Pflug. Arch.* **465**, 1507–1519 (2013).
30. Villalobo, A., Ishida, H., Vogel, H. J. & Berchtold, M. W. Calmodulin as a protein linker and a regulator of adaptor/scaffold proteins. *Biochim Biophys. Acta Mol. Cell Res.* **1865**, 507–521 (2018).
31. Ivanina, T., Blumenstein, Y., Shistik, E., Barzilai, R. & Dascal, N. Modulation of L-type Ca2+ channels by gbeta gamma and calmodulin via interactions with N and C termini of alpha 1C. *J. Biol. Chem.* **275**, 39846–39854 (2000).
32. Liu, Z. & Vogel, H. J. Structural basis for the regulation of L-type voltage-gated calcium channels: interactions between the N-terminal cytoplasmic domain and Ca(2+)-calmodulin. *Front Mol. Neurosci.* **5**, 38 (2012).
33. Beurg, M., Nam, J.-H., Chen, Q. & Fettiplace, R. Calcium Balance and Mechanotransduction in Rat Cochlear Hair Cells. *J. Neurophysiol.* **104**, 18–34 (2010).
34. Corns, L. F., Johnson, S. L., Kros, C. J. & Marcotti, W. Calcium entry into stereocilia drives adaptation of the mechanoelectrical transducer current of mammalian cochlear hair cells. *Proc. Natl. Acad. Sci.* **111**, 14918–14923 (2014).
35. Johnson, S. L., Beurg, M., Marcotti, W. & Fettiplace, R. Prestin-Driven Cochlear Amplification Is Not Limited by the Outer Hair Cell Membrane Time Constant. *Neuron* **70**, 1143–1154 (2011).
36. Fettiplace, R. Hair Cell Transduction, Tuning, and Synaptic Transmission in the Mammalian Cochlea. In Comprehensive Physiology, pp. 1197–1227. https://doi.org/10.1002/cphy.c160049 (2017).
37. Ó Maoiléidigh, D. & Ricci, A. J. A Bundle of Mechanisms: Inner-Ear Hair-Cell Mechanotransduction. *Trends Neurosci.* **42**, 221–236 (2019).
38. Wang, H. et al. Structural basis for modulation of Kv4 K+ channels by auxiliary KChIP subunits. *Nat. Neurosci.* **10**, 32–39 (2007).
39. Pioletti, M., Findeisen, F., Hura, G. L. & Minor, D. L. Jr. Three-dimensional structure of the KChIP1-Kv4.3 T1 complex reveals a cross-shaped octamer. *Nat. Struct. Mol. Biol.* **13**, 987–995 (2006).
40. Gray-Keller, M. P. & Detwiler, P. B. The calcium feedback signal in the phototransduction cascade of vertebrate rods. *Neuron* **13**, 849–861 (1994).
41. Bej, A. & Ames, J. B. Retinal Cyclic Nucleotide-Gated Channel Regulation by Calmodulin. *Int. J. Mol. Sci.* **23**, 14143 (2022).
42. McCoy, A. J. et al. Phaser crystallographic software. *J. Appl. Crystallogr.* **40**, 658–674 (2007).
43. Emsley, P., Lohkamp, B., Scott, W. G. & Cowtan, K. Features and development of Coot. *Acta Crystallogr D. Biol. Crystallogr* **66**, 486–501 (2010).
44. Chen, V. B. et al. MolProbity: all-atom structure validation for macromolecular crystallography. *Acta Crystallogr D. Biol. Crystallogr* **66**, 12–21 (2010).
45. Tamura, K., Stecher, G. & Kumar, S. MEGA11: Molecular Evolutionary Genetics Analysis Version 11. *Mol. Biol. Evol.* **38**, 3022–3027 (2021).
46. Karplus, P. A. & Diederichs, K. Linking crystallographic model and data quality. *Science* **336**, 1030–1033 (2012).

Acknowledgements

We thank beamlines BL18U1, BL19U1, and BL02U1 at Shanghai Synchrotron Radiation Facility (SSRF, China) for X-ray beam time. We thank Dr. Yiquan Tang from Fudan University for sharing the plasmids and helpful discussion. This work was supported by grants from the National Natural Science Foundation of China (22122703, 32100764, 32170767, 32470808, 91953110), the Ministry of Science and Technology of the People's Republic of China (2019YFA0508402), the Major Frontier Research Project of the University of Science and Technology of China (LS9100000002), the Center for Advanced Interdisciplinary Science and Biomedicine of IHM (QYPY20220014), the Strategic Priority Research Program of the Chinese Academy of Sciences (XDB0490000), the Fundamental Research Funds for the Central Universities (WK9100000029), University of Science and Technology of China Research Funds of Double First-Class Initiative (YD9100002006).

Author contributions

Y.L. and C.W. designed the experiments. Y.L., J.C., W.J., and J.Y. performed the experiments. J.C. and X.Z. determined the crystal structure. All authors analyzed the data. Y.L. and C.W. wrote the manuscript. All authors approved the final version of the manuscript. C.W. coordinated the project.

Competing interests

The authors declare no competing interests.

Additional information

Supplementary information The online version contains supplementary material available at https://doi.org/10.1038/s42003-025-07761-1.

Correspondence and requests for materials should be addressed to Chao Wang.

Peer review information *Communications Biology* thanks Ebenezer Yamoah and the other, anonymous, reviewer(s) for their contribution to the peer review of this work. Primary Handling Editors: Janesh Kumar and Laura Rodríguez Pérez.